International Journal of Minerals, Metallurgy and Materials
Volume 25, Number 8, August 2018, Page 937
https://doi.org/10.1007/s12613-018-1643-2

Microstructure refinement and work hardening in a machined surface layer induced by turning Inconel 718 super alloy

Xiao-ping Ren[1,2] *and Zhan-qiang Liu*[1,2]

1) School of Mechanical Engineering, Shandong University, Jinan 250061, China
2) Key Laboratory of High Efficiency and Clean Mechanical Manufacture, Ministry of Education, Shandong University, China
(Received: 9 January 2018; revised: 27 March 2018; accepted: 29 March 2018)

Abstract: The microstructural changes in the machined surface layer of Ni-based super alloys essentially determine the final performance of the structural components of aerospace engines in which these alloys are used. In this work, multiscale metallurgical observations using scanning electron microscopy, electron-backscatter diffraction microscopy, and transmission electron microscopy were conducted to quantitatively characterize the microstructure of the machined subsurface. Next, to elucidate the factors that affect the formation of the refinement microstructure, the distributions of the deformation parameters (strain, strain rate, and temperature) in the machined subsurface were analyzed. A dislocation–twin interaction dynamic recrystallization mechanism for grain refinement during machining of Inconel 718 is proposed. Furthermore, microhardness evolution induced by grain refinement in the machined surface is evaluated. The results suggest that the gradient microstructure and the work hardening can be optimized by controlling the cutting parameters during turning of Inconel 718.

Keywords: grain refinement; dislocation–twin interaction; work hardening; turning; Inconel 718

1. Introduction

Nickel-based superalloys are extensively used in the critical components of aerospace engines and gas turbines because of their excellent properties, which include high fatigue resistance and good thermal stability in severe environments [1–4]. Because of the severe plastic deformation (SPD) imposed on the machined surface during machining, the original surface grain layer is transformed into a depth-dependent microstructure [5–9]. The microstructure can essentially determine various physical mechanical properties in these local regions as well as the final performance of the structural components [7]. Therefore, better knowledge of the underlying mechanism of microstructural changes is critical not only for theoretical understanding but also for technological development of machining techniques for engineering applications. However, unlike the conventional SPD process, for which the deformation mechanism is well understood, the plastic deformation mode of a Ni-based super alloy, which is a low-stacking-fault-energy (SFE) alloy, during cutting remains in the primary stage of experimental observation [8–12]; the mechanisms by which deformations appear are not fully understood, especially at the microscale and nanoscale.

Previous investigations have shown that dislocation slip and deformation twinning are observed as two competitive plastic deformation modes for low-SFE face-centered cubic (fcc) metals and alloys [13–15]. Tao and Lu [16] summarized four different mechanisms for structural refinement of coarse grains with precursor nanoscale deformation twins in fcc metals on the basis of experimental observations of surface mechanical attrition treatments, dynamic plastic deformation, and surface mechanical grinding treatments. The plastic deformation mode is increasingly recognized as being closely associated with not only the extrinsic processing conditions (strain, strain rate, and temperature) but also the intrinsic parameters of original materials (crystal structure, crystal size, and SFE). Chen *et al*. [17] proposed that grain refinement in a Ni-based alloy occurred via formation of mechanical deformation twinning and subsequent interac-

Corresponding author: Zhan-qiang Liu E-mail: melius@sdu.edu.cn

tion of the deformation twinning with dislocations in the surface layer after grinding. However, machining of a metallic alloy as the final processing step of structural components induces high strain (typically 2–10) and high-strain-rate (as high as 10^5 s^{-1}) plastic deformation at the machined surface [18]. The intense, localized, and rapid thermomechanical effect differs substantially from the effects of the aforementioned SPD processes. Consequently, elucidation of the mechanism of microstructure deformation in the deformation layer during cutting remains an urgent need.

Turning is a typical cutting process used for the outside envelope on a turbine disc. An effort was made in the present work to reveal the fundamental mechanism of microstructure refinement in the machined surface layer for Inconel 718 super alloy. The microstructural deformation features of machined samples under different cutting conditions were characterized at the microscale, mesoscopic scale, and nanoscale using scanning electron microscopy (SEM), electron-backscattered diffraction (EBSD), and transmission electron microscopy (TEM). The factors affecting gradient microstructure refinement were revealed by analysis of the strain, strain rate, and temperature of the machined surface under various cutting parameters. On the basis of the experimental observations, a dislocation–twin interaction mechanism of grain refinement during machining of Inconel 718 is proposed. Furthermore, the work hardening in the machined surface was investigated by controlling the cutting parameters to improve the properties of the machined surface.

2. Experimental

2.1. Machining process

The material used in this study was commercial Inconel 718 super alloy made with nominal chemistries (wt%) of 19.28 Cr, 0.72 Al, 0.84 S, 5.55 Nb, 0.99 Ti, 18.10 Fe, and balance Ni. The solution heat treatment was performed at 960°C for 1 h followed by air cooling. The double aging was conducted at 720°C for 8 h, followed by furnace cooling to 620°C at a rate of 50°C/h. The second aging was carried out at 620°C for 8 h, followed by air cooling to room temperature. The initial microstructure of the material is shown in Fig. 1(a). The microstructure is composed of austenitic fcc matrix phase γ and precipitate phases such as γ′ (Ni_3(Al, Ti)), γ″ (Ni_3Nb) (as shown in Fig. 1(b)), and randomly distributed δ particles. The material also contains clusters of primary carbide particles, such as niobium carbide (NbC) and titanium carbide (TiN), as verified by energy-dispersive spectroscopy (Fig. 1(c)).

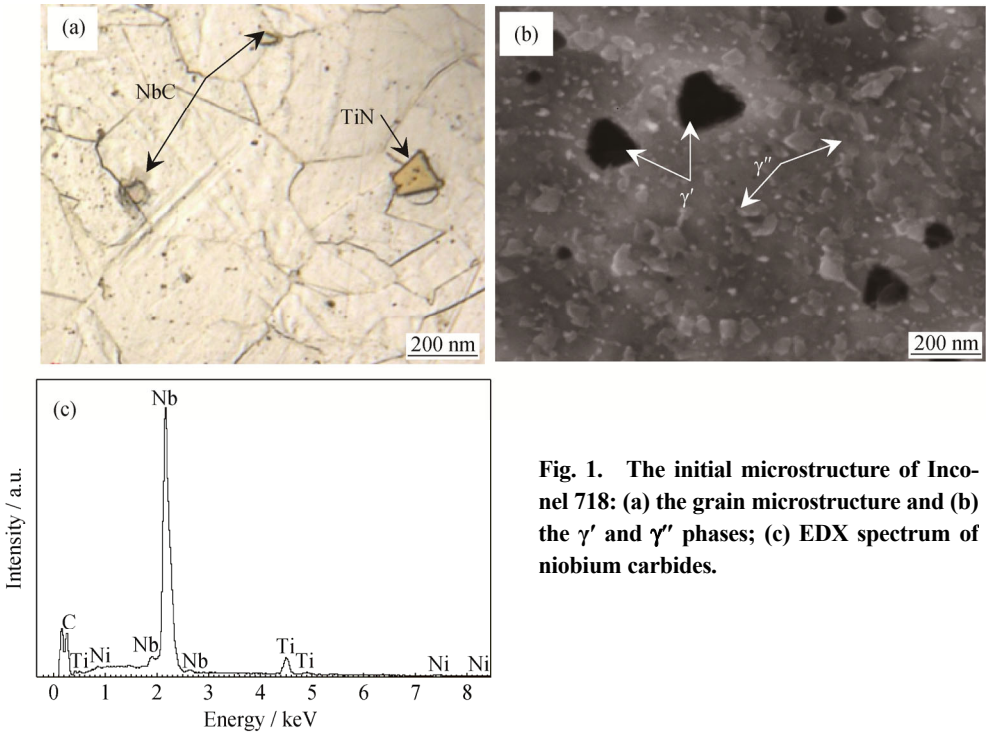

Fig. 1. The initial microstructure of Inconel 718: (a) the grain microstructure and (b) the γ′ and γ″ phases; (c) EDX spectrum of niobium carbides.

The machining process was carried out on a lathe center using a continuously variable spindle rotation speed with a maximum speed of 6000 r/min. Cylindrical specimens 34 mm in diameter and 170 mm in length were fabricated from

a cylindrical forging bar of the alloy. The cutting conditions are given in Table 1. Fig. 2(a) shows a schematic of the turning process. To measure the cutting forces (main cutting force F_c, feed force F_f, and thrust force F_p), a dynamometer (Kistler Inc., model 9257B), a charge amplifier (Kistler Inc., model 5019) and computer software were used. For temperature measurement, an infrared thermal camera (FLUKE Ti400) was used; the camera was mounted approximately 1.2 m behind the machining area. A total of 20–60 frames of the cutting process were recorded for each test, and the highest temperature near the machining zone in each frame was extracted. The average value of the highest temperature in all of the stable cutting frames was calculated. Cross-section of specimens of Inconel 718 machined under different cutting conditions was obtained by wire electrical discharge machining for microstructure observation.

Table 1. Variable operating factors and levels used in machining tests

Cutting speed, v / (m·min^{-1})	Feed rate, f / (mm·r^{-1})	Depth of cut, a_p / mm
50, 70, 90, 110	0.1, 0.15, 0.2	0.2

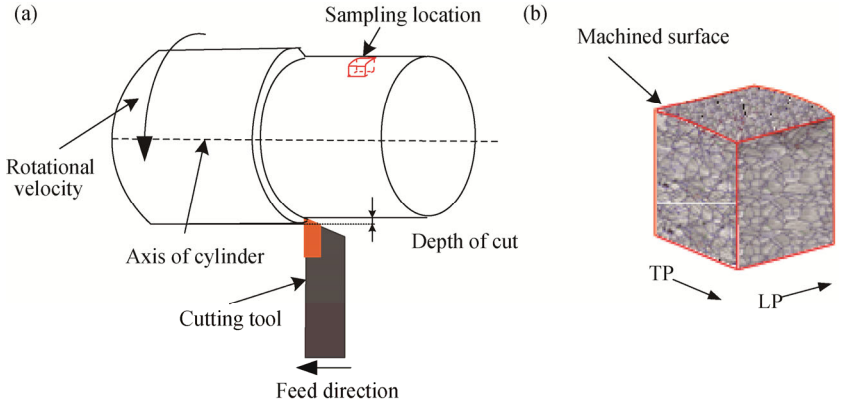

Fig. 2. Schematic of the turning process and sampling location (a) and stereoscopic montage illustrating the measuring direction of the grain structure (b).

2.2. SEM, EBSD, and TEM analyses

The microstructures of the Inconel 718 before and after the machining processing were examined using SEM (JEOL 6335F), EBSD (JOEL JSM-7800F), and TEM (Tecnai G2 F20 S-TWIN). Cross-sections of the samples were prepared for observation of the microstructural evolution from the machined surface to the interior of the specimen. For SEM and EBSD examinations, samples after mechanical polishing (with SiC to 2000 grit) were electrolytically etched using a mixture of hydrochloric and nitric acids to reveal the microstructure. For the TEM analysis, the samples were prepared by focused-ion beam milling to produce a sufficiently thin ample (4 μm (length) × 4 μm (height) × 100 nm (thickness)) perpendicular to the plane of the machined surface. In the TEM analysis conducted at an accelerating voltage of 200 kV, selected-area electron diffraction (SAED) techniques were used to characterize the samples.

According to the American Society for Testing and Materials standards [19], the effect of the cutting speed on grain refinement was evaluated in the transverse plane (TP) and the effect of the feed rate on grain refinement was evaluated in the longitudinal plane (LP), as shown in Fig. 2(b). The test area with at least 500 grains was used to evaluate the average grain size. Furthermore, to explore the microstructure from the microscale perspective, the dislocation densities were estimated using Eq. (1), where the total dislocation density ρ_{tol} is proportional to the strain gradient [20]:

$$\rho_{tol} = \frac{4\gamma}{b\lambda} \tag{1}$$

where b is the Burgers vector, γ is the macroscopic plastic shear strain, and λ is the local length scale of the deformation field.

2.3. Microhardness

Microhardness measurements were obtained by the Vickers micro-indentation hardness testing method with a diamond indenter subjected to a load of 0.49 N. The full load was applied for 8 s. The measurement of microhardness was performed into the depth of the material along a straight line perpendicular to the machined surface (circular-shaped). The first point of microhardness measurement was located as far as 15 μm from the machined surface, depending on the profile hump or caving, as shown in Fig. 3. The successive measurements were performed at 10-μm intervals until the hardness of the bulk material was obtained.

The bulk microhardness was measured 3 mm below the machined surface. One of the issues associated with microhardness measurements is sensitivity to hard particles just below the workpiece surface. To circumvent this issue, a series of measurements were taken and the averages of the measurements were obtained.

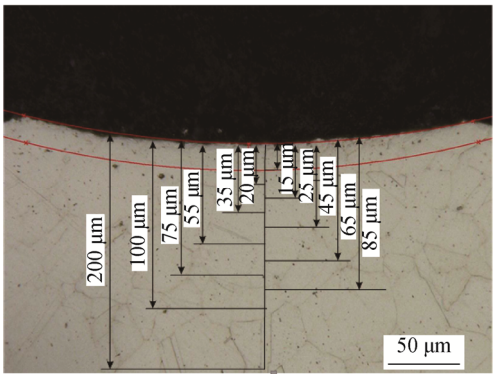

Fig. 3. Optical analysis of a specimen with an indication of the levels of microhardness.

3. Results and discussion

3.1. Microstructure for undeformed Inconel 718

An EBSD image of the original microstructure structure on the undeformed region of an Inconel 718 super alloy sample is shown in Fig. 4. Figs. 4(a) and 4(b) show the orientation imaging microscopy (OIM) map of the undeformed material, which was composed of equiaxed grains and a certain amount of annealing twins. The average grain size of the initial microstructure was approximately 34.6 μm. The grain boundaries represented by the red lines in Fig. 4(a) were identified as Σ3 twin boundaries (TBs) (TBs, <111>/60°) [21], confirming the existence of annealing twins. The corresponding inverse pole figure (IPF) orientation map constructed from the TP direction is shown in Fig. 4(b). Judging from the corresponding {100}, {110}, and {111} pole figures (Fig. 4(c)), the texture of the analyzed region was determined to be {011} <211>, a typical weak brass texture in fcc metals.

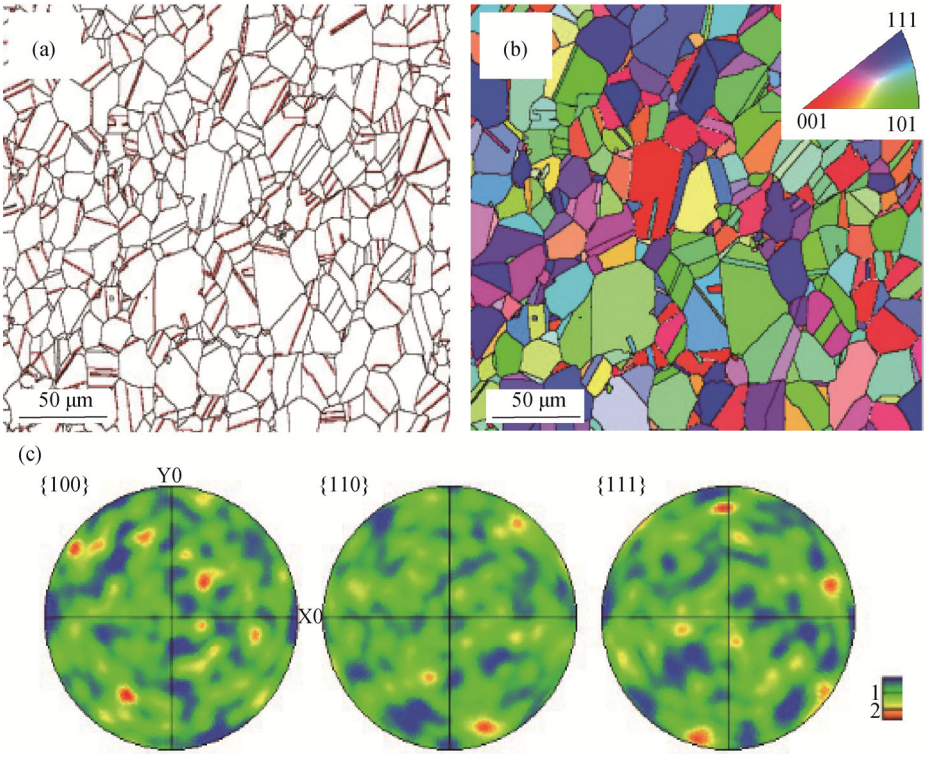

Fig. 4. Original microstructure of Inconel 718: (a) distribution of annealing twinning boundaries (red lines); (b) OIM map, including the corresponding IPF orientation map constructed from the TP direction; (c) {100}, {110}, and {111} pole figures.

3.2. Microstructure of the deformation layer

3.2.1. Machined subsurface deformation layer

Fig. 5(a) shows a cross-sectional microstructure topography in the subsurface deformation layer taken in the LP at a cutting speed of 90 m/min, as observed by SEM. The observed gradient microstructure observed in the turned samples can be divided into two regions: the 0–150 μm subsurface grain refinement layer, and the bulk material. EBSD images were selected to detect the microstructure transformation of the selected regions in the machined surface layer (red rectangle in Fig. 5(a)) for microscopic observation. A deformed elongated grain, fragmentation grain,

microcracks, and microcavities are clearly observed in the subsurface deformation layer, as shown in Fig. 5(b), collectively demonstrating that plastic deformation occurred. By contrast, in the very-near-surface deformation layer, the grains can hardly be distinguished because the thickness of several microns was actually not probed by the EBSD method because of technical limitations. Furthermore, profuse deformation twinning was observed in the surface layer (indicated by red lines in Fig. 5(b)), which was evidently incremental compared with the original annealed structure (Fig. 4(a)). Similar observations have been reported for other low-SFE fcc materials subjected to the SPD process [21]. A comparison of the pole figures of the subsurface deformation layer with those of the initial microstructure (Fig. 4(c)) reveals a typical shear-induced deformation texture (see Fig. 5(d)); this observation correlates well with previous observations of machined copper, which is a typical low-SFE metal [22]. This shear-induced deformation texture is caused by the shearing process dominating the material removal process during cutting [23].

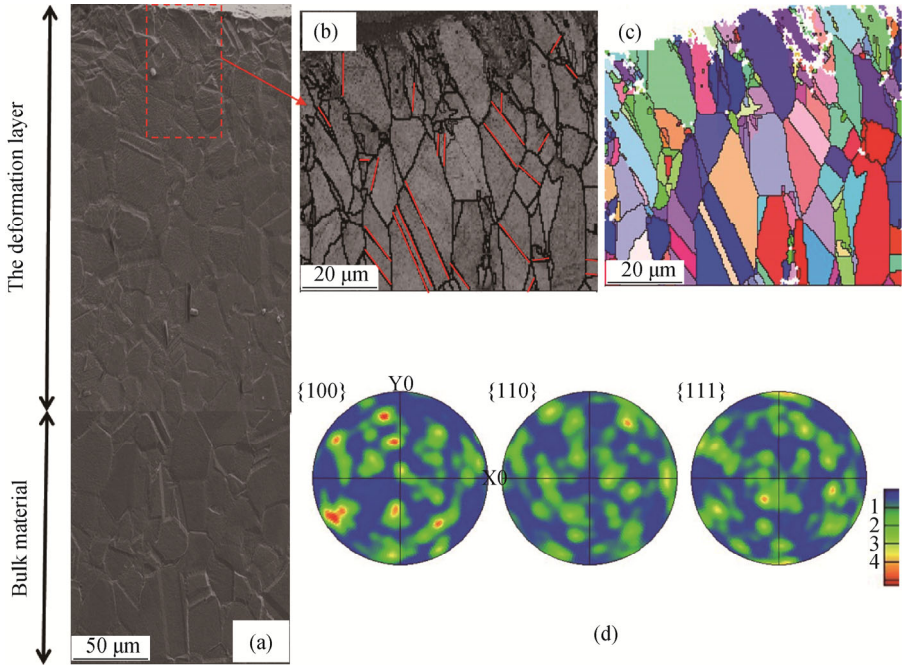

Fig. 5. Analysis of subsurface deformation layer: (a) cross-sectional SEM image showing the microstructure of the subsurface deformation layer; (b) EBSD magnified images of the region inside the red rectangle in (a); (c) the corresponding OIM map; (d) {100}, {110}, and {111} pole figures.

To elucidate the microstructural features of the deformation layer, the SPD zone in the very near surface was observed by TEM (Fig. 6). Whereas equiaxed grains were observed in the initial microstructure (Fig. 4(a)), obvious slip bands (Fig. 6(a)) were generated along the cutting speed direction in the subsurface deformation layer. Moreover, SAED analysis of the SPD zone showed an overlapping feature (Fig. 6(a)), demonstrating that nanometer-sized grains formed because the surface material underwent plastic deformation at a very high strain rate (estimated to be approximately 10^4 to 10^5 s^{-1}). The cross-sectional microstructure variation along the depth was observed using high-magnification TEM images, as shown in Figs. 6(b) and 6(c). Compared with the deformation microstructure at relatively low strain (Fig. 6(c)), even more dislocations, including dislocation cells and network dislocations, were formed during higher-strain plastic deformation (Fig. 6(b)). In the present case, the maximum strain gradient of 0.2 μm^{-1} corresponds to a ρ_{tol} maximum value of 3.2×10^{15} m^{-2}, which is much higher than the dislocation density of (9.6×10^{13} m^{-2}) bulk microstructure.

High-resolution TEM (HRTEM) observations were carried out to identify the structural characteristics of samples at the nanoscale. Fig. 7 shows the cross-sectional HRTEM images of the deformation structures in the very-near-surface deformation layer along the <110> zone axis. Specifically, for nanotwin lamellae in the rectangular region at the top (blue rectangle), at least three types of dislocations near the TBs—full dislocation, partial dislocation, and dislocation pile-up (indicated by blue, black, and yellow arrows, respectively)—are observed (Fig. 7(b)). Moreover, TBs were actually stepped rather than planar at the atomic level. For the rectangular region at the bottom (red rectangle), a thinned twin lamella is well distinguished (Fig. 7(c)), with full dislocation and dislocation pile-up near the nanotwin lamella. From the fast Fourier transformation (FFT) (Fig. 7(c), inset), a misorientation angle of 21.8° along the <110> zone axis is

observed among these lamellae. The fragmentation of nanotwin lamellae was actually induced by dislocation–twin interactions; the detailed process and underlying mechanism will be discussed in Section 3.4.

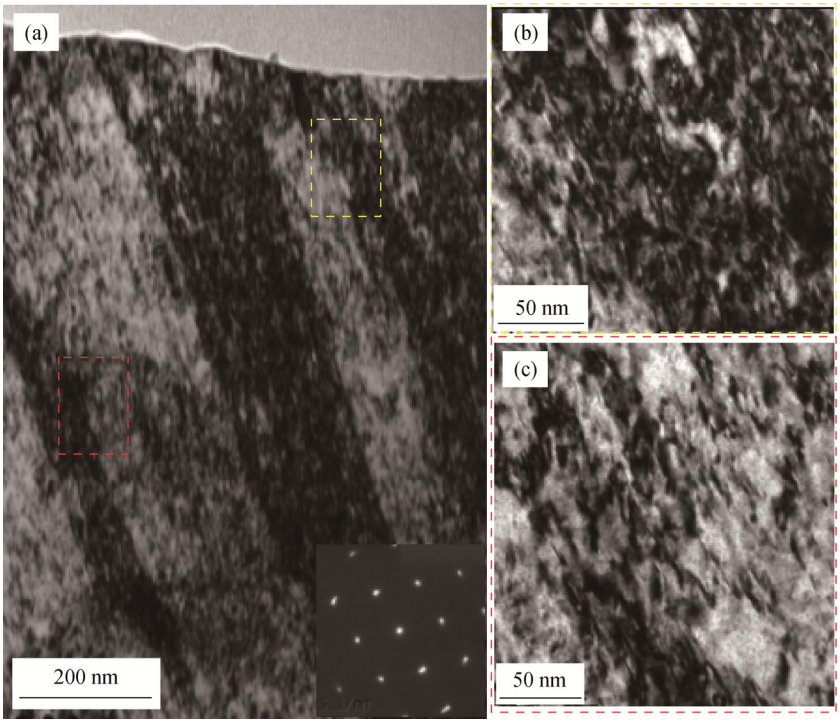

Fig. 6. Cross-sectional TEM images of the top surface layer and the corresponding SAED pattern (bottom right) (a), and the magnified images corresponding to the yellow and red rectangles in (a) are shown in (b) and (c), respectively.

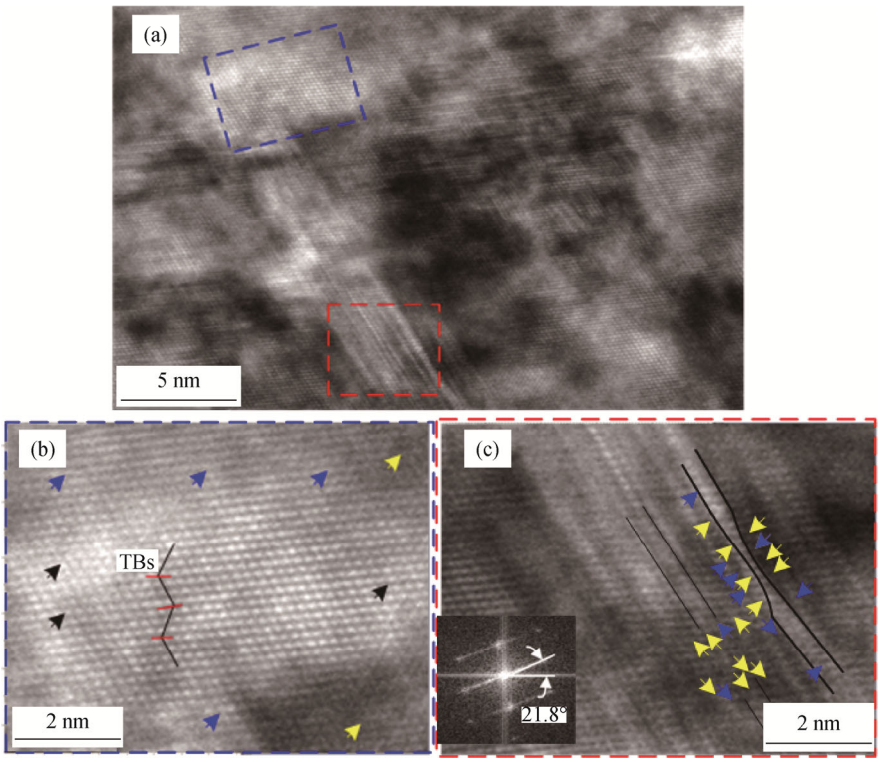

Fig. 7. Cross-sectional HRTEM images of the top surface: (a) HRTEM images showing the microstructure in the deformation layer; (b) the magnified images corresponding to the blue rectangular region in (a); (c) the magnified images corresponding to the red rectangular region in (a) with the FFT image in the bottom left. Full dislocations, partials, and dislocation pile-up are labeled by blue, black, and yellow arrows, respectively.

3.2.2. Influence of the cutting parameters

The grain morphology and average grain size distributions of the subsurface along the depth beneath the surface for different feed rates and cutting speeds are shown in Figs. 8 and 9, respectively. The location of the samples (indicated by the red rectangle) and the measuring direction (LP) of the grain structure under different feed rates are shown in Fig. 8(a). The average grain sizes as a function of depth in the samples in the LP with three feed rates (f = 0.1 mm/r, 0.15 mm/r, 0.2 mm/r) are summarized in Fig. 8(b). The average grain sizes were calculated on the basis of EBSD measurement data, where 15 μm was taken as the interval along the depth. The distribution curves show that the grain size refinement further intensified along the depth when the feed rate was increased from 0.1 mm/r to 0.2 mm/r. Compared with the grain morphology of the bulk material (Fig. 1(a)), grain refinement is observed in Figs. 8(c)–8(e) after machining; in addition, the average grain size decreased with increasing feed rate. The average values of the grain size (D_{avg}) were 30.89 μm, 22.22 μm, and 20.48 μm, corresponding to feed rates of 0.1 mm/r, 0.15 mm/r, and 0.2 mm/r, respectively. Furthermore, the statistical results of grain diameters are displayed in Figs. 8(c)–8(e). The volume fractions of small grains (less than 20 μm) were 31%, 51.5%, and 52.5% for the three feed rates of 0.1 mm/r, 0.15 mm/r, and 0.2 mm/r, respectively. The statistical results of the grain sizes indicate that the degree of grain refinement increases with increasing feed rate.

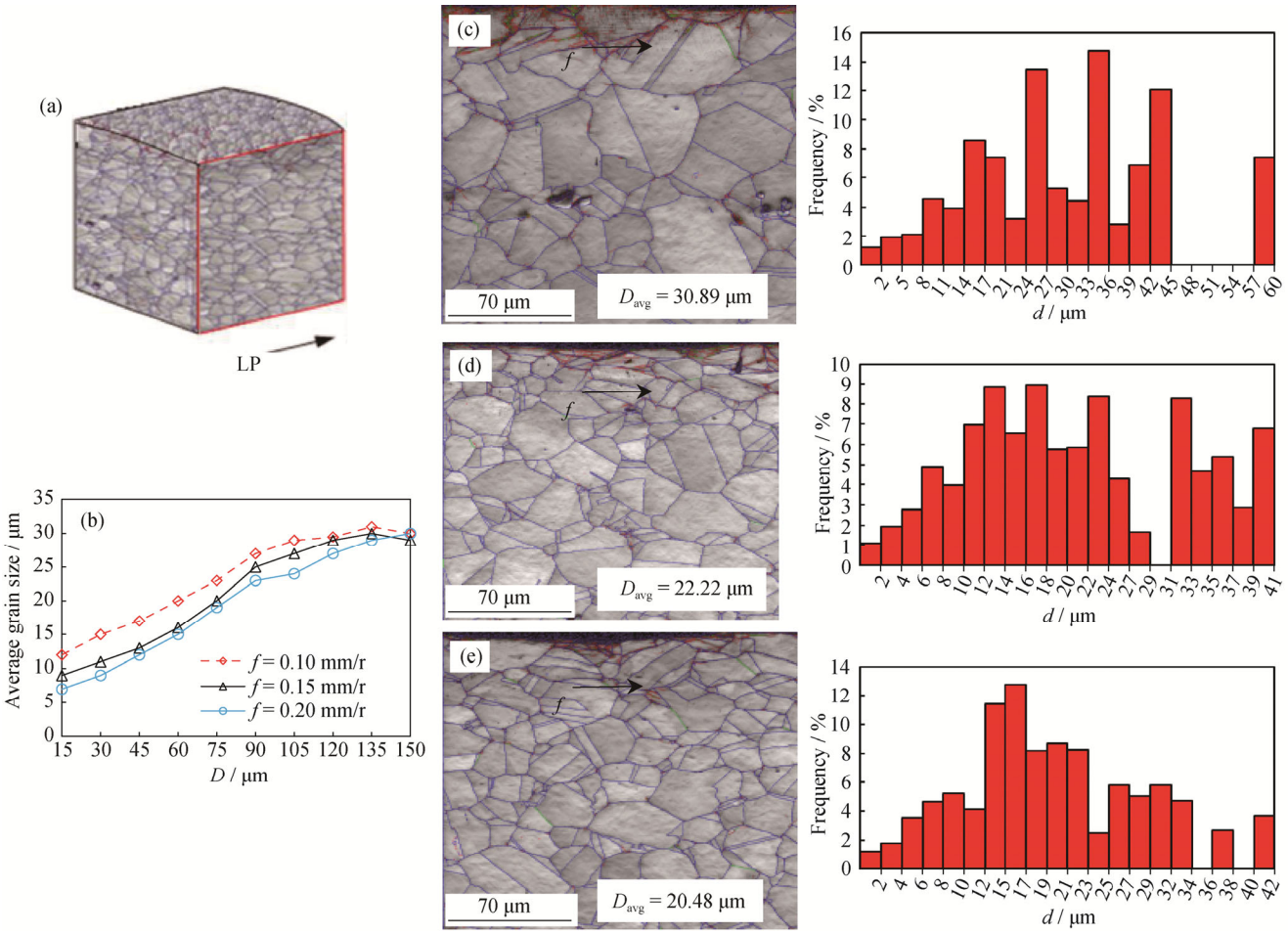

Fig. 8. The influence of feed rates on grain morphology and grain size distribution of the subsurface: (a) the red rectangle illustrating the measuring direction (LP) of the grain structure; (b) grain size distributions of the alloy along the depth with different feed rates; (c,d,e)the grain morphology and grain size distribution of the subsurface((v = 90 m/min, a_p = 0.2 mm, f = 0.1, 0.15, 0.2 mm/r).

Fig. 9(a) shows the location of samples (indicated by a red rectangle) and measuring direction (TP) of the grain structure under different cutting speeds. The average grain size distributions of the subsurface along the depth in the LP with four cutting speeds (v = 50 m/min, 70 m/min, 90 m/min, 110 m/min) are shown in Fig. 9(b). With an increase

in the cutting speed from 50 m/min to 110 m/min, the grain size refinement further intensified along the depth. Furthermore, Figs. 9(c)–9(f) show that, with an increase in cutting speed from 50 m/min to 110 m/min, the average grain sizes decrease from 23.69 μm to 14.04 μm. The statistical results of grain diameters are also displayed in Figs. 9(c)–9(f). The volume fractions of small grains (less than 20 μm) were 21.5%, 65%, 55.5%, and 74% for the four cutting speeds of 50 m/min, 70 m/min, 90 m/min, and 110 m/min, respectively. The statistical results of grain sizes reveal that the degree of grain refinement first increases and then decreases with increasing cutting speed. The refined grains tend to grow under the effect of high cutting temperature at a cutting speed of 90 m/min.

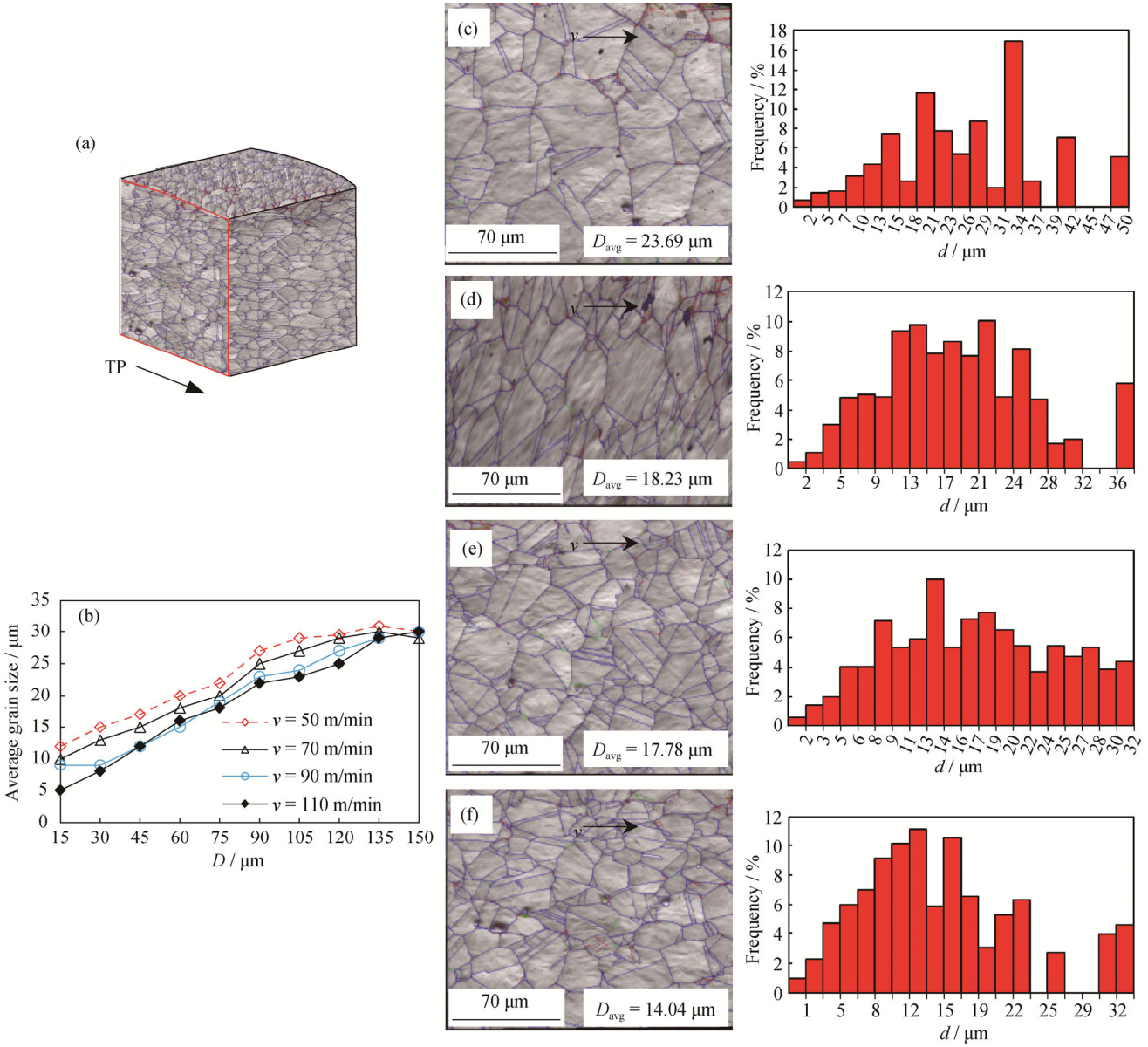

Fig. 9. The influence of cutting speeds on grain morphology and grain size distribution of the subsurface: (a) the red rectangle illustrating the measuring direction (TP) of the grain structure; (b) grain size distributions of the alloy along the depth, as plotted for different cutting speeds; (c,d,e,f) the grain morphology and grain size distribution of the subsurface (f = 0.2 mm/r, a_p = 0.2 mm, v = 50, 70, 90, 110 m/min)

Notably, dynamically recrystallized grains were observed in the machined surface layer, as shown in Figs. 8(d) and 8(e) and Figs. 9(d)–9(f). A similar phenomenon has been previously observed in the near-surface layer of the machined specimens of Inconel 718 turned using coated cutting tools at different cutting speeds (60–90 m/min) [7]. This phenomenon is caused by the heavy plastic deformation at extremely high strain rates during the machining process,

which leads to the mechanical work being converted into heat. Although the heat may partially flow into the substrate and the surroundings, the temperature rise was substantial; the effects led to the occurrence of dynamically recrystallized grains. Dynamically recrystallized grains have also been previously observed in Ni-based super alloys as an important grain refinement mechanism when the grain size was refined to the micrometer range [24]. However, dynamic recrystallization (DRX) by SPD appears to fail to account for refined grains at the nanometer scale. A modified grain refinement mechanism will be discussed in detail in Section 3.4.

3.3. Quantification of deformation levels in the machined surface layer

To quantitatively analyze the deformation parameters, e.g., strain, strain rate, and temperature, three-dimensional turning simulations were conducted using the ABAQUS software, where the cutting conditions were simulated in accordance with the experiments. In the simulations, a curved workpiece geometry was modeled as viscoelastic and was represented by a large number of elements (40000). The friction between the tool and the workpiece was described by a hybrid model that includes shear friction and Coulomb friction along the rake and flank faces of the tool. The heat transfer coefficient $h = 10^5$ N/(s·mm·K) between the tool and workpiece was used to reach the steady-state temperature field within a short time period [25]. All three-dimensional turning simulations were run until full chip formation occurred at a fixed cutting length. Finally, the deformation parameters (strain, strain rate, and temperature) were extracted from the simulation results. The cutting model was verified by comparing the predicted cutting forces and temperature with the measured cutting forces and temperature, as shown in Table 2. From Table 2, the total average error was 16.23% for the cutting force and 13.53% for the cutting temperature, both of which were in the acceptable range.

Table 2. Variable operating factors and levels used in the machining tests

Condition	Forces	Prediction / N	Measurement / N	Error / %	Measured T_{max} / °C	Predicted T_{max} / °C	Error / %
v = 50 m/min,	F_p	117.73	148.2	20.5			
f = 0.1 mm/r,	F_c	139.98	172.6	18.9	595	695	14.4
a_p = 0.2 mm	F_f	66.50	77.5	14.2			
v = 70 m/min,	F_p	126.42	151.4	16.5			
f = 0.15 mm/r,	F_c	176.54	206.0	14.3	600	710	15.5
a_p = 0.2 mm	F_f	54.66	66.5	17.8			
v = 70 m/min,	F_p	180.61	207.6	13.0			
f = 0.2 mm/r,	F_c	177.15	208.9	15.2	740	840	11.9
a_p = 0.2 mm	F_f	49.36	58.0	14.9			
v = 90 m/min,	F_p	119.60	141.2	15.3			
f = 0.1 mm/r,	F_c	138.52	165.3	16.2	640	730	12.3
a_p = 0.2 mm	F_f	47.81	58.3	18.0			

Fig. 10 illustrates the variation in the effective strain, strain rate, and temperature along the depth of the machined surfaces of Inconel 718 for four cutting speeds (v = 50 m/min, 70 m/min, 90 m/min, 110 m/min) and three feed rates (f = 0.1 mm/r, 0.15 mm/r, and 0.2 mm/r). The plots show that a very high rate of shear deformation with a high strain gradient, high strain rate gradient, and a large temperature gradient were applied on the surface of Inconel 718, where refinement microstructures were induced. In the top surface layer of 150 μm thickness, the estimated strain rate varies from 10^3 to 10^5 s^{-1} and the accumulative equivalent strains range from 0.2 to 4.5, with the corresponding strain gradients varying from 0.01 to 0.1 μm^{-1}. The maximum temperature of the top surface was 700–800°C, with a temperature gradient of 5.33°C/μm across the thickness of the surface layer.

Deformation at high strain rates may suppress the dislocation annihilation kinetics and facilitate the formation of more grain boundaries or dislocation boundaries [26]. Furthermore, the strain gradient in plastic deformation is proportional to the density of the stored geometrically necessary dislocations [27]. The much larger strain gradients in the surface layer of Inconel 718 indicate that a much higher geometrically necessary dislocation is generated. In addition, the dislocation activities are depressed at lower temperatures; therefore, finer grains are expected for plastic defor-

mation at higher temperatures. This prediction is related to the observation of the microstructure in the subsurface of Inconel 718 during machining. Therefore, the gradient distribution features of the extrinsic processing parameters (strain, strain rate, temperature, etc.) along the depth below the surface were responsible for the gradient microstructure.

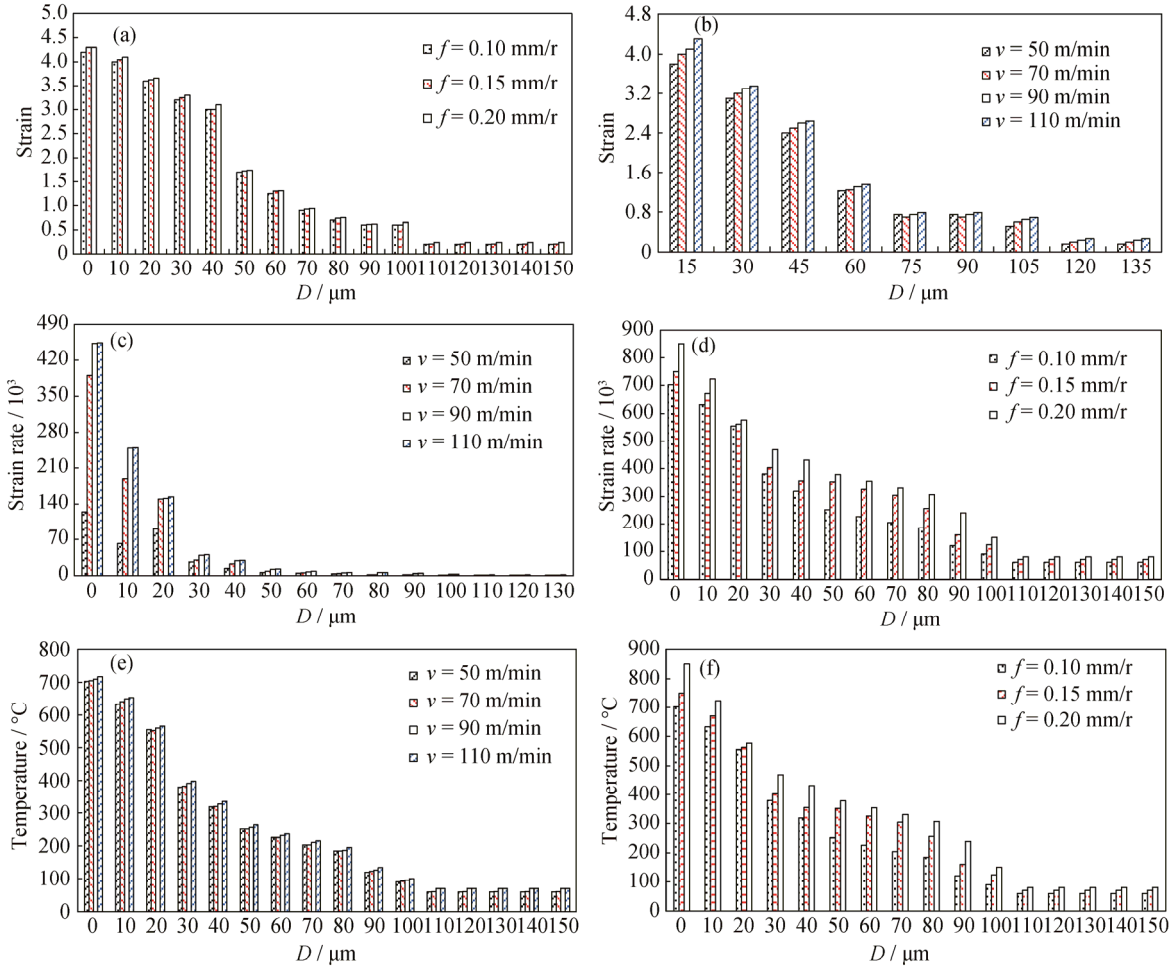

Fig. 10. Variation of strains (a, b), strain rates (c, d), and temperature (e, f) vs. distance beneath the machined surface at different cutting speeds (f = 0.15 mm/r, a_p = 0.2 mm) and feed rates (v = 70 m/min, a_p = 0.2 mm).

3.4. Dislocation–twin interaction and grain refinement

The intrinsic parameters of the original materials (crystal structure, crystal size, stacking fault energy, etc.) were determining factors for the plastic deformation mode for Inconel 718. From the microstructure features in terms of the experimental observations, various dislocations in refinement grains and a nonuniform distribution of deformation twinning were detected throughout the deformed layer. In particular, in the very near surface layer, many randomly distributed full and partial dislocations are observed at or near nanotwin boundaries (Fig. 7), forming stepped or distorted TBs. These results demonstrate that deformation twinning and dislocation activities are two competitive processes in the grain refinement process.

For fcc metals with a low SFE, the onset of twinning occurs when the twinning stress, σ_T, becomes equal to or less than the slip stress, σ_S. Otherwise, the slip response dominates [28]. The slip response was modeled via the Zerilli–Armstrong constitutive description (Eq. (2)), which captures the essential physical phenomena. A Hall–Petch relationship accounting for the effect of grain size can be ascribed to the twinning stress, as expressed by Eq. (3).

$$\sigma_S = C_0 + C_1 \cdot \varepsilon^n \cdot \exp\left(-C_2 T + C_3 \cdot \ln \dot{\varepsilon}\right) + k_S \cdot d^{-1/2} \quad (2)$$

$$\sigma_T = k\left(\frac{\gamma_{sf}}{G \cdot b_S}\right)^{1/2} + k_T \cdot d^{-1/2} \quad (3)$$

where d is grain diameter; C_0, C_1, C_2, C_3 are material constants; k_s is the contant for sliping; ε is the equivalent plastic strain; $\dot{\varepsilon}$ represents the equivalent strain rate; T is the absolute temperature of the workpiece; k is the proportionality constant; G is the shear modulus; b_S is the Burgers vector of

a partial dislocation; γ_{sf} is the stacking fault energy of the material; k_T is the Hall–Petch slope for twinning. For Inconel 718 with a low SFE, in which twinning easily occurred, fragmentation of twin/matrix (T/M) lamellae was regarded as a precursor process to nanoscale refinement of coarse grains in fcc metals [29]. With increasing strain and strain rate, the dislocations were accumulated within the thin T/M layers or at numerous TBs. The accommodation of more dislocations at TBs resulted in a gradual loss of their coherency, and the T/M lamellae fragmented into refined grains. Furthermore, when induced strain in the workpiece reached a critical level, i.e., critical strain ε_r, DRX started. For Inconel 718 super alloy, we adopted the ε_r for the initiation of DRX proposed by Jafarian *et al*. [30], who amended the model of Samantaray *et al*. [31] by calibration constant c; the critical strain can be expressed as Eq. (4):

$$\varepsilon_r = \left(0.00234\dot{\varepsilon}^{0.1298}\exp\left[\frac{5759.863}{T+273}\right]\right)/c \tag{4}$$

On the basis of the aforementioned deformation analysis of the machined surface, the appearance of a gradient microstructure in the machined surface layer is attributed to the gradient deformation parameters (Fig. 5). Furthermore, the appearance of a gradient microstructure is controlled through selection of appropriate cutting parameters.

To more intuitively describe the grain refinement induced by the dislocation–twin interaction during machining, the formation and breaking process of nanotwins in [011]-oriented nanograins is illustrated in Fig. 11. Initially, the plastic deformation is governed by twinning, which divided the original coarse grains into finer twin lamellae. As the machining process continues, the slip system of the nanograin with the largest Schmidt factor is first activated. Full or partial dislocations then initiate from the sample surface or grain boundary and successively glide on the adjacent or nonadjacent {111} planes. As shown in the Thompson tetrahedron [32], high-density dislocation arrays are formed within the twin platelets (Fig. 11(b)). The activated partial dislocations slip successively toward and interact with TBs, resulting in final breakage of the nanotwin lamella (Fig. 11(c)). Simultaneously, the heavy plastic deformation at a high strain rate also increases the temperature of the sample. When the temperature is higher than the recrystallization temperature, DRX occurs (Fig. 11(d)). Because of DRX, nanosized grains form in the regions near the topmost surface, where the highest strain is generated during turning (Fig. 11(e)).

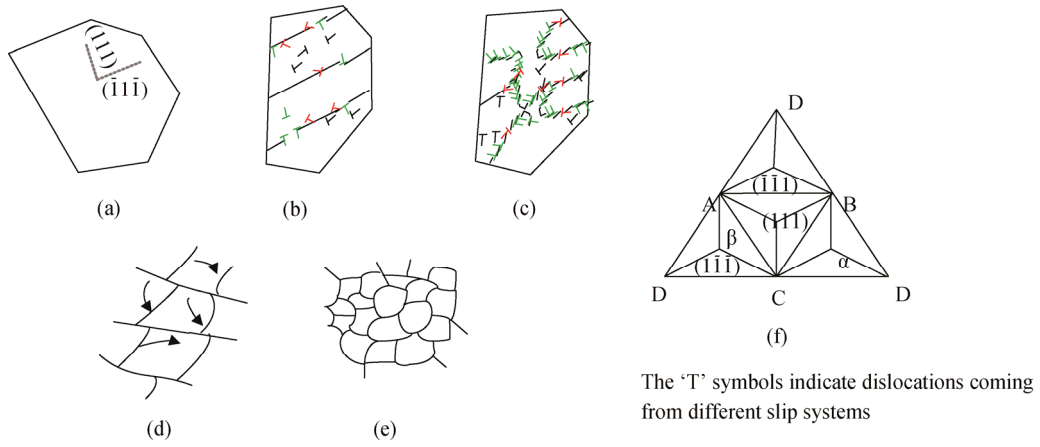

Fig. 11. Schematic showing the formation and breaking process of nanotwins in the {011}-oriented nanograins during turning: (a) undeformed grain; (b) occurrence of dislocations; (c) dislocation arrangement; (d) rotation of subgrains; (e) grain refinement; (f) Thompson tetrahedron.

3.5. Microhardness evolution induced by grain refinement in the machined surface

Fig. 12 shows the changes in microhardness with the distance from the surface developed under the cutting conditions. The Vickers hardness measurement data show that, at a depth from 15 to 100 μm, the hardness varies from HV 462 ± 4.5 to HV 383 ± 3.5, depending on the cutting parameters.

Remarkable hardening in metals and alloys induced by plastic deformation processing can be attributed to grains being refined to the sub-micrometer or nanometer scale, to stored dislocation density, and to an orders-of-magnitude increase in microtwinning. According to the Hall–Petch relationship [33], the smaller the grain size is, the greater the hardness. In addition, the presence of substructures inside the deformation layer, such as the dislocations and TBs revealed in HRTEM observations (Fig. 7), provide additional hardening. In particular, in the case of Inconel 718 super al-

loy, its higher percentages of niobium and chromium strengthen the grain boundaries through the formation of complex metallic carbides such as M_6C (Fig. 1), thereby impeding dislocation movement and inducing greater plastic deformation. Apart from complex carbides, the Inconel 718 alloy also contains a large volume of uniformly distributed γ′ precipitates—the main strengthening phase in solution-treated Inconel 718. Hence, shear deformation during the chip formation of the Inconel 718 alloy becomes difficult, which ultimately leads to a work-hardening effect.

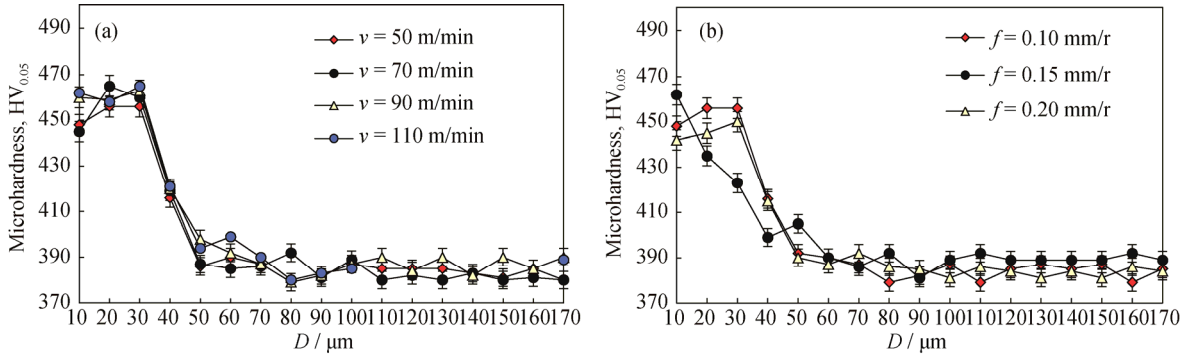

Fig. 12. Variation of the microhardness along the depth beneath the machined surface for different cutting speeds (a) (f = 0.2 mm/r, a_p = 0.2 mm) and different feed rates (b) (v = 90 m/min, a_p = 0.2 mm).

4. Conclusions

(1) Because of a gradient in the variation of the strain and strain rate from the treated top surface (both are extremely large) to the deep matrix (essentially zero), a gradient in the grain size distribution, from a few nanometers in the top surface layer to several micrometers in the deep matrix, was developed in the samples. Various degrees of grain refinement were observed in the surface layer machined under different feed rates and cutting speeds (50 m/min ≤ v ≤ 110 m/min), 0.1 mm/r ≤ f ≤ 0.2 mm/r). Furthermore, the average grain size was strongly affected by the cutting parameters (cutting speed and feed rate). The degree of grain refinement was found to intensify with increasing feed rate (from 0.1 mm/r to 0.2 mm/r) and increasing cutting speed (from 50 m/min to 110 m/min). Higher deformation parameters (strain, strain rate, and temperature) induced by higher cutting speeds and feed rates resulted in much finer grains in the subsurface layer.

(2) The plastic deformation mode of Inconel 718 was found to be determined not only by the extrinsic processing conditions (strain, strain rate, temperature, etc.) but also by the intrinsic parameters of the original material (crystal structure, crystal size, stacking fault energy, etc.). The accumulation of dislocations around nanotwin lamellae, TBs, and separated nanotwin fragments in the topmost surface nanograins provided direct evidence of grain refinement induced by dislocation–twin interaction. The detailed process, including deformation twinning, dislocation–twin reaction, localized thinning of nanotwin lamellae, and subsequent DRX, was outlined.

(3) Remarkable hardening in Inconel 718 induced through the manufacturing process was attributed to the grains being refined to sub-micrometer or nanometer scales and the stored dislocation density as well as microtwinning being pumped up by orders of magnitude. The surface property can be enhanced through selection of the appropriate cutting parameters.

Acknowledgements

The authors would like to acknowledge the financial support from the National Natural Science Foundation of China (No. 51425503) and the Major Science and Technology Program of High-end CNC Machine Tools and Basic Manufacturing Equipment of China (No. 2014ZX04012014). This work was also supported by a grant from the Taishan Scholar Foundation of Shandong province (No. TS20130922).

References

[1] A. Thakur and S. Gangopadhyay, State-of-the-art in surface integrity in machining of nickel-based super alloys, *Int. J. Mach. Tools Manuf.*, 100(2016), p. 25.

[2] D. Ulutan and T. Ozel, Machining induced surface integrity in titanium and nickel alloys: A review, *Int. J. Mach. Tools Manuf.*, 51(2011), No. 3, p. 250.

[3] I.S. Jawahir, E. Brinksmeier, R.M'Saoubi, D.K. Aspinwall, J.C. Outeiro, D. Meyer, D. Umbrello, and A.D. Jayal, Surface integrity in material removal processes: Recent advances, *CIRP Ann.*, 60(2011), p. 603.

[4] C.W. Dai, W.F. Ding, J.H. Xu, C. Ding, and G.Q. Huang,

Investigation on size effect of grain wear behavior during grinding nickel-based superalloy Inconel 718, *Int. J. Adv. Manuf. Technol.,* 91(2017), No. 5-8, p. 2907.

[5] W.F. Ding, L.C. Zhang, Z. Li, Y.J. Zhu, H.H. Su, and J.H. Xu, Review on grinding-induced residual stresses in metallic materials, *Int. J. Adv. Manuf. Technol.*, 88(2017), No. 9-12, p. 2939.

[6] W.F. Ding, B. Linke, Y.J. Zhu, Z. Li, Y.C. Fu, H.H. Su, and J.H. Xu, Review on monolayer CBN superabrasive wheels for grinding metallic materials, *Chin. J. Aeronaut.*, 30(2017), No. 1, p. 109.

[7] R. M'Saoubi, T. Larsson, J. Outeiro, Y. Guo, S. Suslov, C. Saldana, and S. Chandrasekar, Surface integrity analysis of machined Inconel 718 over multiple length scales, *CIRP Ann.*, 61(2012), No. 1, p. 99.

[8] J. Gubicza, L. Farbaniec, G. Csiszár, T. Sadat, H. Couque, and G. Dirras, Microstructure and strength of nickel subjected to large plastic deformation at very high strain rate, *Mater. Sci. Eng. A*, 662(2016), p. 9

[9] A.M. Wusatowska-Sarnek, B. Dubiel, A. Czyrska-Filemonowicz, P.R. Bhowal, N.B. Salah, and J.E. Klemberg-Sapieha, Microstructural characterization of the white etching layer in icnkel-based superalloy, *Metall. Mater. Trans. A*, 42(2011), p. 3813.

[10] X.C. Liu, H.W. Zhang, and K. Lu, Strain-induced ultrahard and ultrastable nanolaminated structure in nickel, *Science*, 342(2013), No. 6156, p. 337.

[11] M. Imran, P.T. Mativenga, A. Gholinia, and P.J. Withers, Evaluation of surface integrity in micro drilling process for nickel-based superalloy, *Int. J. Adv. Manuf. Technol.*, 55(2011), No. 5-8, p. 465.

[12] D.A. Huges and N. Hansen, Microstructure and strength of nickel at large strains, *Acta Mater.*, 48(2000), No. 11, p. 2985.

[13] N.R. Tao, X.L. Wu, M.L. Sui, J. Lu, and K. Lu, Grain refinement at the nanoscale via mechanical twinning and dislocation interaction in a nickel-based alloy, *J. Mater. Res.*, 19(2004), p. 1623.

[14] S. Asgari, E. El-danaf, S.R. Kalidindi, and R.D. Doherty, Strain hardening regimes and microstructural evolution during large strain compression of low stacking fault energy fcc alloys that form deformation twins, *Metall. Mater. Trans. A*, 28(1997), No. 9, p. 1781.

[15] S. M′Guil, W. Wen, S. Ahzi, J.J. Gracio, and R.W. Davies, Analysis of shear deformation by slip and twinning in low and high/medium stacking fault energy fcc metals using the φ-model, *Int. J. Plast.*, 68(2015), p. 132.

[16] N.R. Tao and K. Lu, Nanoscale structural refinement via deformation twinning in face-centered cubic metals, *Scripta Mater.*, 60(2009), No. 12, p.1039.

[17] Y.X. Chen, Y.Q. Yang, Z.Q. Feng, B. Huang, X. Luo, and G.M. Zhao, Grain refinement and texture evolution during high precision machining of a Ni-based superalloy, *Philos. Mag.*, 97(2017), No. 1, p.28.

[18] D. Gao, Z.P. Hao, R.D. Han, Y.L. Chang, and J.N. Muguthu, Study of cutting deformation in machining nickel-based alloy Inconel 718, *Int. J. Mach. Tools Manuf.*, 51(2011), No. 6, p. 520.

[19] B. Mather and S. F. Etris, *American Society for Testing and Materials (ASTM)*. Springer, US, 1981, p. 8.

[20] M.F. Ashby, The deformation of plastically non-homogeneous materials, *Philos. Mag.*, 21(1969), No. 170, p. 399.

[21] M. Kumar, A.J. Schwartz, and W.E. King, Microstructural evolution during grain boundary engineering of low to medium stacking fault energy fcc materials, *Acta Mater.*, 50(2002), No. 10, p. 2599.

[22] I.J. Beyerlein and L.S. Tóth, Texture evolution in equal-channel angular extrusion, *Prog. Mater. Sci.*, 54(2009), No. 4, p. 427.

[23] S. Swaminathan, M.R. Shankar, S. Lee, J. Hwang, A.H. King, R.F. Kezar, B.C. Rao, T.L. Brown, S. Chandrasekar, W. Dale Compton, and K.P. Trumble, Large strain deformation and ultra-fine grained materials by machining, *Mater. Sci. Eng. A*, 410-411(2005), p. 358.

[24] S.C. Medeiros, Y.V.R.K. Prasad, W.G. Frazier, and R. Srinivasan, Microstructural modeling of metadynamic recrystallization in hot working of IN 718 superalloy, *Mater. Sci. Eng. A*, 293(2000), No. 1-2, p. 198.

[25] A.D. Prete, L. Filice, and D. Umbrello, Numerical simulation of machining nickel-based alloys, *Procedia CIRP*, 8(2013), p. 540.

[26] N.R. Tao, Z.B. Wang, W.P. Tong, M.L. Sui, J. Lu, and K. Lu, An investigation of surface nanocrystallization mechanism in Fe induced by surface mechanical attrition treatment, *Acta Mater.*, 50(2002), No. 18, p. 4603.

[27] K. Shizawa, K. Kikuchi, and H.M. Zbib, A strain-gradient thermodynamic theory of plasticity based on dislocation density and incompatibility tensors, *Mater. Sci. Eng. A*, 309-310(2001), p. 416.

[28] H. Jarmakani, Y.M. Wang, E. Bringa, and M.A. Meyers, Modeling of the slip-twinning transition in nanocrystalline nickel and nickel-tungsten under shock compression, *Shock Compression of Condensed Matter*, 24-29(2007), p. 239.

[29] K. Wang, N.R. Tao, G. Liu, J. Lu, and K. Lu, Plastic strain-induced grain refinement at the nanometer scale in copper, *Acta Mater.*, 54(2006), No. 19, p. 5281.

[30] F. Jafarian, M.I. Ciaran, D. Umbrello, P.J. Arrazola, L. Filice, and H. Amirabadi, Finite element simulation of machining Inconel 718 alloy including microstructure changes, *Int. J. Mech. Sci.*, 88(2014), p. 110.

[31] D. Samantaray, S. Mandal, M. Jayalakshmi, C.N. Athreya, A.K. Bhaduri, and V.S. Sarma, New insights into the relationship between dynamic softening phenomena and efficiency of hot working domains of a nitrogen enhanced 316L(N) stainless steel, *Mater. Sci. Eng. A*, 598(2014), p. 368.

[32] Y.T. Zhu, X.L. Wu, X.Z. Liao, J. Narayan, L.J. Kecskés, and S.N. Mathaudhu, Dislocation-twin interactions in nanocrystalline fcc metals, *Acta Mater.*, 59(2011), No. 2, p. 812.

[33] G.D. Hughes, S.D. Smith, C.S. Pande, H.R. Johnson, and R.W. Armstrong, Hall-Petch strengthening for the microhardness of twelve nanometer grain diameter electrodeposited nickel, *Scripta Metall.*, 20(1986), No. 1, p. 93.